

# Engineering, control and longitudinal readout of Floquet qubits

Anthony Gandon,<sup>1,2</sup> Camille Le Calonnec,<sup>1</sup> Ross Shillito,<sup>1</sup> Alexandru Petrescu,<sup>1</sup> and Alexandre Blais<sup>1,3</sup>

<sup>1</sup>*Institut Quantique and Département de Physique,*

*Université de Sherbrooke, Sherbrooke, Québec, J1K 2R1, Canada*

<sup>2</sup>*Mines ParisTech, PSL Research University, F-75006 Paris, France*

<sup>3</sup>*Canadian Institute for Advanced Research, Toronto, M5G1M1 Ontario, Canada*

Properties of time-periodic Hamiltonians can be exploited to increase the dephasing time of qubits and to design protected one and two-qubit gates. Recently, Huang *et al.* [Phys. Rev. Applied **15**, 034065 (2021)] have shown that time-dependent Floquet states offer a manifold of working points with dynamical protection larger than the few usual static sweet spots. Here, we use the framework of many-mode Floquet theory to describe approaches to robustly control Floquet qubits in the presence of multiple drive tones. Following the same approach, we introduce a longitudinal readout protocol to measure the Floquet qubit without the need of first adiabatically mapping back the Floquet states to the static qubit states, which results in a significant speedup in the measurement time of the Floquet qubit. The analytical approach developed here can be applied to any Hamiltonian involving a small number of distinct drive tones, typically the study of standard parametric gates for qubits outside of the rotating-wave approximation.

## I. INTRODUCTION

Realizing the promises of quantum computing requires the ability to manipulate and measure complex states of quantum devices with high fidelity. An outstanding challenge towards reaching this goal is the realization of fast and high-fidelity entangling gates with large on-off ratio. An approach to turn on and off entangling interactions is to frequency tune pairs of qubits in and out of resonance. However, noise in the control parameter allowing to tune the qubit frequency introduces an additional source of dephasing, which can be mitigated by operating the qubits at sweet spots where they are first-order insensitive to this noise channel [1].

In superconducting qubits such as the transmon [2], tuning the qubit frequency is most commonly accomplished by threading a loop with magnetic flux. While for static dc flux bias there are a few sweet spots per single flux period  $\Phi_0$ , it was recently shown that tailored ac modulation of the flux or direct voltage drive on the qubits extends these few static sweet spots to a larger class of dynamical sweet spots [3–7]. This gives more flexibility in choosing the operating points to both maximize dephasing times and facilitate two-qubit gates.

In the presence of a continuous ac drive, the static computational basis of the qubits is replaced by a set of eigenstates of the periodic Floquet Hamiltonian, also known as Floquet states. Protocols for initialization, readout, single-qubit operations and entangling gates on these Floquet qubits have been theoretically proposed [3] and experimentally investigated [8] showing improvements in the dephasing time of the qubits. Floquet qubits can be frequency-tuned in large frequency range by changing the parameters of the drive. This tunability can be used, for example, to implement single-qubit phase gates, but also to bring together pairs of Floquet qubits to activate SWAP-type interactions [3]. On the other hand, for X-type single-qubit gates, or for two-qubit gates such as the cross-resonance [9], a second drive is introduced to induce

transitions between the Floquet-qubit states [3]. Moreover, as shown in Refs. [3, 8], the readout of the Floquet qubit can be performed in a two-step process: the Floquet qubit is first mapped to the laboratory-frame qubit by adiabatically turning off the drive. At that point, a usual dispersive readout is performed by driving a cavity coupled to the qubit [10].

In this work, we exploit the Many-Mode Floquet theory (MMFT) introduced in Refs. [11–13] to provide an analytical description of the dynamics of the Floquet qubit during such gates, which involve more than one drive frequency. Generalized spectra describing the system during the operation of the gate can be used to optimize gate parameters, as well as to understand the dynamics of higher-energy states.

Using this approach, which allows for multiple simultaneous drives, we also show how it is possible to use a driven coupler to engineer a longitudinal interaction between the Floquet qubit and a readout cavity. Thanks to both the longitudinal nature of this interaction – which is known to lead to fast qubit measurements [14] – and to the fact that there is no need to map the Floquet qubit back to the undriven qubit states before the readout, we find from numerical simulations that this approach can lead to fast and high-fidelity Floquet qubit readout. A superconducting circuit design for this longitudinal Floquet readout is proposed.

The paper is structured as follows. In Sec. II, we review the Floquet and MMFT frameworks. In Sec. III we show how X-type gates can be implemented on Floquet states by adding a second drive to the qubit and we apply MMFT to the driven Floquet qubits during the gate. We then demonstrate the feasibility of dynamical longitudinal readout of Floquet states with an additional drive in Sec. IV, and compare our analytical results to full numerics. Finally, in Sec. V we explore the timescales necessary for the initialization of a Floquet qubit.

## II. FLOQUET FRAMEWORK

### A. Floquet qubits

Driven quantum systems are part of a larger class of systems evolving under a time-periodic Hamiltonian with period  $T = 2\pi/\omega_d$  and which are efficiently described by the Floquet formalism [15, 16], where a system Hamiltonian  $H_s$  with Hilbert-space dimension  $d$  is replaced with the time-dependent Floquet Hamiltonian (with  $\hbar = 1$ ):

$$H_F(t) = H_s + V(t) - i \frac{\partial}{\partial t}, \quad (1)$$

with  $V(t) = V(t+T)$  the periodic drive on the system. Based on the symmetry of the Hamiltonian  $H_F$  under time translation  $t \rightarrow t+T$ , the Floquet theorem states the existence of a full set of solutions to the time-dependent Schrodinger equation so that  $\forall t, H_F(t) |\psi_n(t)\rangle = 0, (n = 1, 2, \dots, d)$ . To complete the analogy with the static Hamiltonian, these solutions are related to the eigenvalue problem for the Floquet Hamiltonian  $\forall t, H_F(t) |\phi_n(t)\rangle = \epsilon_n |\phi_n(t)\rangle, (n = 1, 2, \dots, d)$  with:

$$\forall t, \forall n \leq d, |\psi_n(t)\rangle = e^{-i\epsilon_n t} |\phi_n(t)\rangle, \quad (2)$$

where the *Floquet modes*  $|\phi_n(t)\rangle$  are  $T$ -periodic in time, and the *quasienergies*  $\epsilon_n$  are real-valued coefficients which are invariant under translation by multiples  $k$  of the drive frequency  $\omega_d$ . The term *quasienergies* thus refers to representatives of equivalence classes, often chosen in the first Brillouin zone  $[-\omega_d/2, \omega_d/2]$ . With appropriately designed driving protocols, one can convert an undriven Hamiltonian  $H_s$  into the dressed  $H_F(t)$  and continuously map the energies to the quasienergies and the eigenstates to the corresponding Floquet states, hence the name *Floquet qubit* when the time-dependent dressed states are used to define the two-level system.

In this context, dynamical protection consists of operating the Floquet qubit at extrema of the quasienergy difference with respect to the drive parameters subject to noise [3, 4, 6]. As shown by Huang *et al.* [3], dynamical sweet spots represent manifolds in parameter space, in contrast with the few isolated static sweet spots that are found in the absence of a drive. This allows for an increased freedom in the parameter choice that can be used to operate the Floquet qubit while being protected from low-frequency noise, which translates to high coherence times. This property is compatible with single and two-qubit gate operations, which justifies the promising role Floquet qubits could play in quantum information processing.

### B. Many-Mode Floquet Theory

Floquet qubits describe a subgroup of driven systems evolving under the dynamics of a  $T$ -periodic Hamiltonian

as introduced in Eq. (1). Here, the Hamiltonian often includes the effect of only one drive on a static system or else multiple drives at different harmonics of one characteristic frequency. In some cases such as certain gates on Floquet qubits, one can face Hamiltonians with two distinct time-dependent terms:

$$H_F(t) = H_s + V_1(t) + V_2(t) - i \frac{\partial}{\partial t}, \quad (3)$$

with  $V_1, V_2$  respectively  $2\pi/\omega_1$  and  $2\pi/\omega_2$  periodic in time. The Floquet qubit is generated by the first driving term and the system Hamiltonian, while the second term is typically only switched on during the gate without any *a priori* link between the frequencies  $\omega_1$  and  $\omega_2$ . We will limit ourselves to two distinct frequencies and their harmonics, even if the scheme used in studies of Hamiltonians with multiple drives is more general [17–21].

In the rotating-wave approximation (RWA), the two distinct frequencies typically result in a single effective frequency on the system at the difference  $(\omega_1 - \omega_2)$ , but Floquet analysis aims at describing the dynamics of driven systems without such simplification. We first notice that the extension of Floquet theory to commensurate frequencies is straightforward using the greatest common divisor  $\omega_{\text{GCD}} = \text{GCD}(\omega_1, \omega_2)$  as the new frequency of a single-tone Floquet system for the duration of the gate [22]. This result translates into the definition of Floquet states and quasienergies for Eq. (3) which create the continuous connection between Floquet states before and after the gate. These intermediary states can be numerically evaluated, but complexity arises as the new period of the system can be orders of magnitude greater than the distinct timescales  $2\pi/\omega_1$  and  $2\pi/\omega_2$ . In practice, this leads to long simulation times.

A generalization of these ideas for multiple incommensurate frequencies exists under the name of Many-Mode Floquet Theory [16, 23, 24]. The main idea here is to look for a generalization of the  $N$  Floquet states and quasienergies by considering a Fourier basis with two dimensions rather than only one:

$$\forall n \leq N, |\phi_n(t)\rangle = \sum_{k_1, k_2} e^{i(k_1\omega_1 + k_2\omega_2)t} |\phi_{n, k_1, k_2}\rangle \quad (4)$$

$$\forall n \leq N, \epsilon_{n, k_1, k_2} = \epsilon_{n, 0, 0} + k_1\omega_1 + k_2\omega_2. \quad (5)$$

MMFT has been implemented into a numerical solver using truncated Fourier bases [25], which we do not make use of in this work. However, the generalization of quasienergies and Floquet Modes provides an analytical approach to understand the dynamics of driven systems with additional drives such as naturally occurs in Floquet qubits.

## III. SINGLE-QUBIT OPERATIONS

Approaches to realize  $X, \sqrt{X}$  and single-qubit phase gates on Floquet qubits were proposed in Ref. [3] with

Fidelities obtained from numerical simulations exceeding 99.99% and gate durations on the order of tens of nanoseconds. Our focus here is on the  $X$  and  $\sqrt{X}$  gates based on adding a secondary drive to the Floquet qubit to induce Rabi oscillations between the Floquet states.

We extend the principle of the Floquet spectrum to driven Floquet qubits, widely used in static systems with a single drive frequency. This approach has recently been used by Petrescu *et al.* [26] to extract gate parameters maximizing the gate rate while minimizing higher order  $ZZ$ -terms. The generalized Floquet spectrum is defined with respect to the second drive frequency acting on the periodic Floquet System, typically the drive inducing a  $X$ -Gate on a Floquet qubit. We characterize the generalized avoided crossings appearing at resonances in the spectrum of the Floquet qubit.

### A. X-Gate in the RWA

We use as logical states the eigenstates of a two-level system (TLS) and, without loss of generality, we will set a transition frequency  $\omega_0/2\pi = 5.02$  GHz and a near-resonant Rabi drive with amplitude  $\varepsilon_{d1}/2\pi = 0.21$  GHz and with a detuning  $\Delta = \omega_0 - \omega_{d1}$ :

$$H(t) = \frac{\omega_0}{2}\sigma_z + \varepsilon_{d1}\cos(\omega_{d1}t)\sigma_x. \quad (6)$$

Going to a frame rotating at  $\omega_{d1}$  and applying the RWA by assuming  $\varepsilon_{d1} \ll \omega_{d1}$ , the Floquet states and quasienergies of the Hamiltonian of Eq. (6) take the form:

$$\begin{aligned} \epsilon_{0,1} &= \pm\sqrt{\left(\frac{\Delta}{2}\right)^2 + \varepsilon_{d1}^2}, \\ |\phi_{0,1}(t)\rangle &= \frac{e^{+i\omega_{d1}t/2}}{\sqrt{\varepsilon_{d1}^2 + (\epsilon_{0,1} - \frac{\Delta}{2})^2}} \begin{pmatrix} |\varepsilon_{d1}|e^{-i\omega_{d1}t} \\ \epsilon_{0,1} - \frac{\Delta}{2} \end{pmatrix}. \end{aligned} \quad (7)$$

Further imposing  $|\Delta| \ll \varepsilon_{d1}$ , the Floquet states  $|\phi_{0,1}\rangle$  are located near the equatorial plane of the Bloch sphere. Following Huang *et al.* [3], the addition of a second drive along the  $Z$ -axis in the laboratory frame with a frequency  $\omega_{d2}$  chosen close to the quasienergy difference induces Rabi oscillations of the Floquet qubit. With this addition the Hamiltonian now reads:

$$H(t) = \frac{\omega_0}{2}\sigma_z + \varepsilon_{d1}\cos(\omega_{d1}t)\sigma_x + \varepsilon_{d2}\cos(\omega_{d2}t)\sigma_z, \quad (8)$$

where  $\varepsilon_{d2}$  is the amplitude of the second drive. As an example, for a transmon qubit, a drive along the  $Z$  axis is realized by flux pumping the qubit's SQUID loop [2].

In Fig. 1(a) we plot results from an integration of the Schrödinger equation showing a full population transfer between the states  $|\phi_0(t)\rangle, |\phi_1(t)\rangle$  with fidelity 99.99% and ramp times of the order of 20 ns, corresponding to the pulses represented in Fig. 1(b). There, the green curve corresponds to the amplitude  $\varepsilon_{d1}$  of the first drive and is used to establish the Floquet logical states. A second,

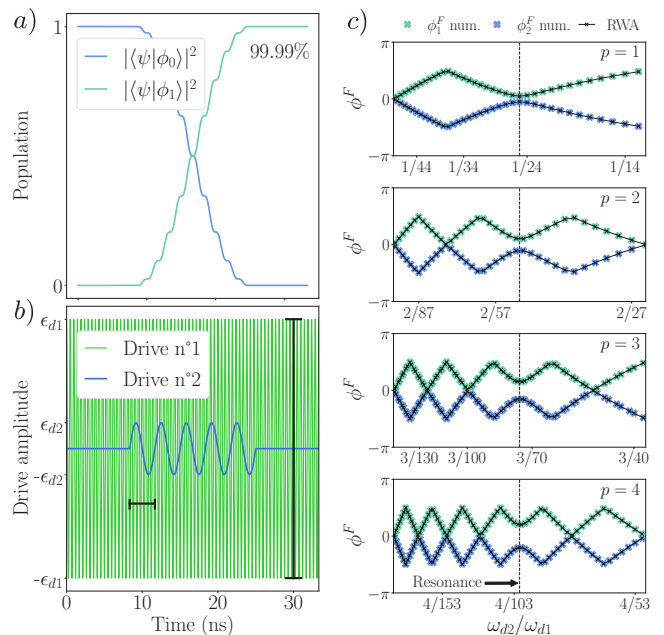


FIG. 1. a) Population of the Floquet modes  $|\phi_0(t)\rangle$  and  $|\phi_1(t)\rangle$  as a function of time under the Hamiltonian Eq. (8). b) Typical drive amplitude as a function of time. The first drive  $\varepsilon_{d1}$  (green line) is used to generate the Floquet qubit states while the second drive  $\varepsilon_{d2}$  (blue line) drives Rabi oscillations between these levels. c) Four quasiphase spectra for different numerators  $p = 1, 2, 3, 4$  in the ratio  $\omega_{d2}/\omega_{d1} = p/q$ . The colored dots are obtained from diagonalization of the propagator associated with Eq. (8) after a common period  $2\pi/\omega_{\text{GCD}}$  and by sweeping the values of  $q$ . Because of the folded space, several crossings are observed. However, a unique anticrossing corresponding to the resonance of the second drive with the Floquet qubit is observed (vertical line).

flux, tone (blue curve) is switched on for the duration of the gate and its frequency  $\omega_{d2}$  is close to twice the amplitude  $\varepsilon_{d1}$  of the Floquet qubit drive.

The analysis in this section relies on the RWA and is therefore only valid in the limit  $|\Delta| \ll \varepsilon_{d1}$ . An analogous application of the RWA would be further necessary when treating the second drive, for example in order to express the gate rate of the Floquet-qubit X-gate. Corrections beyond the RWA, applicable also in the more general case of off-resonant drives can be derived [27]. Instead, in the following subsection we rely on the exact Floquet two-tone numerical method to obtain the gate rate.

### B. Two-tone Floquet analysis

Here, we propose an alternative approach to analyze a gate on the Floquet states based on a two-tone Floquet analysis. A Floquet spectrum is obtained from the Hamiltonian of Eq. (8) with respect to the second drive frequency  $\omega_{d2}$  without requiring any of the previous RWAs. To do so, we regroup the time-dependent

terms into a single quasi-periodic drive  $V(t)$ . If the frequencies  $\omega_{d1}$  and  $\omega_{d2}$  are commensurate, then the periodicity of  $V(t)$  is given by the greatest common divisor  $\omega_{\text{GCD}} = \text{GCD}(\omega_{d1}, \omega_{d2})$ .

In the presence of two tones, the quasienergy spectrum is probed by sweeping one of the drive frequencies. However, because the quasienergies are only defined modulo  $\omega_{\text{GCD}}$  and because this quantity will strongly depend on the chosen  $\omega_{d2}$ , it is not possible to define a continuous quasienergy spectrum.

As explained in Sec. II, when the drive frequencies can be written as an irreducible fraction  $\omega_{d1}/\omega_{d2} = p/q$ , the frequency  $\omega_{\text{GCD}}$  can be expressed as  $\omega_{\text{GCD}} = \omega_{d1}/p = \omega_{d2}/q$ . Here,  $\omega_{d1}$  is taken as a fixed parameter such that each numerator  $p$  corresponds to a distinct first Brillouin zone. For each numerator  $p$ , we can introduce a discrete quasienergy spectrum satisfying  $\omega_{d2} = \omega_{d1} \times q/p$  for  $q \in \mathbb{N}$ . To compare quasienergy spectra corresponding to different numerators  $p$ , we normalize the Floquet quasienergy spectrum  $\epsilon_{1/2}(\omega_{d2})$  defined over the range  $[-\omega_{\text{GCD}}/2, \omega_{\text{GCD}}/2]$  to obtain the Floquet quasiphase spectrum defined as  $\phi_{1/2}^F(\omega_{d2}) = \epsilon_{1/2}(\omega_{d2}) \times 2\pi/\omega_{\text{GCD}}$  over  $[-\pi, \pi]$ .

In Fig. 1(c), we plot the quasiphase spectra associated with the Hamiltonian Eq. (8) for commensurate ratios  $\omega_{d2}/\omega_{d1}$  with small numerators. The different subplots illustrate the discrete quasiphase spectra for different values of the numerator  $q$ . The difference between the two quasiphases  $\phi_1^F$  and  $\phi_2^F$  exhibits a local minimum over all the subplots around  $\omega_{d2}/\omega_{d1} \approx 0.04$  which is linked to an avoided crossing characterizing the resonance of the second drive with the Floquet qubit and thus yields the gate rate. The analytical approximation obtained in the previous subsection shows good agreement when the parameter choice satisfies the RWA conditions. A precise numerical estimate of the size of this anticrossing, valid without any RWA, is obtained by increasing the maximum allowed numerator at the cost of longer simulations. A detailed procedure for extracting the local minimum corresponding to the avoided crossing can be found in Appendix A. Notably, we mitigate the need for intensive numerical simulations by taking advantage of Dysolve [28], a recent semi-analytic solver capturing the effects of oscillatory terms in the system Hamiltonian and whose performances are discussed in Appendix A.

The validity of the approach presented here goes beyond the two-level approximation used in this work and can easily be extended to, for example, the higher energy levels of Floquet qubits.

#### IV. LONGITUDINAL FLOQUET QUBIT READOUT

We now turn to the readout of the Floquet qubit. In Refs. [3, 8, 29], this is realized by adiabatically mapping the Floquet logical states back to the original undriven

qubit states, followed by a usual dispersive qubit readout [10]. This two-step process, adiabatic mapping following by readout, leads to a longer measurement time than strictly necessary. Here, we introduce an approach to directly measure the Floquet qubit without the additional step of an adiabatic mapping. Moreover, we show how it is possible to engineer a longitudinal coupling between the Floquet qubit and a readout mode by using a modulated transversal coupling. Because of its longitudinal nature, this readout can reach a large signal-to-noise ratio (SNR) in a measurement time that is small compared to the usual dispersive readout of circuit QED [14]. This approach bears similarities with the stroboscopic measurements of Ref. [30] and the Kerr-cat qubit readout of Ref. [31].

##### A. Engineered longitudinal coupling

Our approach is based on the usual capacitive, or transversal, coupling between a laboratory-frame qubit and a readout cavity. In the laboratory frame, the Hamiltonian reads

$$H_{\text{lab}}(t) = \frac{\omega_0}{2}\sigma_z + \varepsilon_{d1} \cos(\omega_1 t)\sigma_x + \omega_r \hat{a}^\dagger \hat{a} + g(t)(\hat{a} + \hat{a}^\dagger)\sigma_x, \quad (9)$$

where we have added to the driven qubit (first two terms) a cavity of frequency  $\omega_r$  and annihilation operator  $\hat{a}$  coupled to the qubit with a strength  $g(t)$  which we allow to be time-dependent. In the regime where the detuning between the drive and the qubit  $\Delta$  is small compared to the drive amplitude  $\varepsilon_{d1}$ , the laboratory frame  $\sigma_x$  acts as  $\sigma_z$  on the Floquet qubit corresponding to a longitudinal coupling to the cavity mode.

To make this more apparent, we move to the interaction frame defined by the transformation

$$U(t; 0) = e^{-i\omega_r t \hat{a}^\dagger \hat{a}} \sum_{j \in \{0,1\}} |\phi_j(t)\rangle \langle \phi_j(0)| e^{-i\epsilon_j t}, \quad (10)$$

where, in the limit  $\Delta/\varepsilon_{d1} \ll 1$ , the interaction-picture Hamiltonian takes the form

$$H_{\text{int}}(t) \approx g(t) \cos(\omega_0 t)(\hat{a} e^{i\omega_r t} + \hat{a}^\dagger e^{-i\omega_r t})\sigma_z^F(0). \quad (11)$$

Here, we have introduced the interaction-picture Pauli matrices  $\sigma_k^F(t)$  with  $k = x, y, z$  acting on the basis of the Floquet modes  $\{|\phi_0(t)\rangle, |\phi_1(t)\rangle\}$ . Choosing the time-dependent coupling to be of the form  $g(t) = \tilde{g} \cos(\omega_m t)$  with a modulation frequency  $\omega_m = \omega_r - \omega_0$  (and/or  $\omega_r + \omega_0$ ) yields the longitudinal coupling Hamiltonian [14]

$$H_{\text{int}}(t) \approx \frac{\tilde{g}}{2}(\hat{a} + \hat{a}^\dagger)\sigma_z^F(0). \quad (12)$$

As discussed in Ref. [14], evolution under this Hamiltonian leads to an optimal separation of the cavity pointer states where the initial cavity vacuum state is displaced 180 degrees out of phase depending on the state of the qubit.

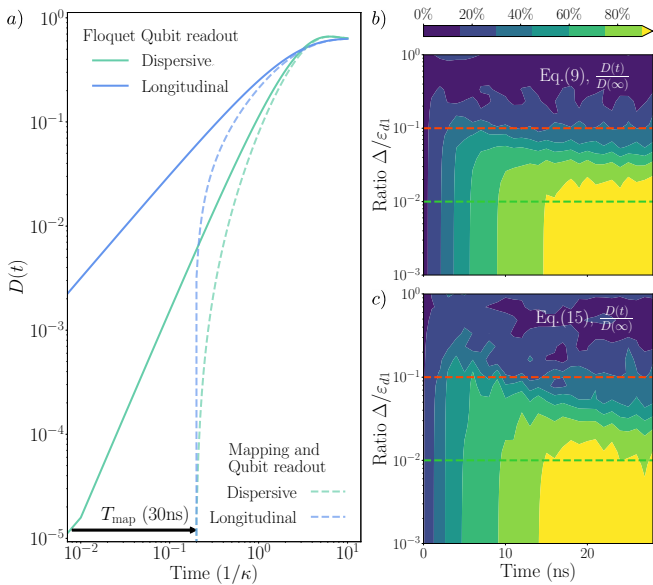


FIG. 2. a) Pointer-state separation  $D(t)$  as a function of time for longitudinal Floquet readout (full blue line), dispersive readout without state mapping (full green line), dispersive readout with the necessary state mapping with a ramp time of  $T_{\text{map}} = 30$  ns (dashed green line). b) Pointer state separation  $D(t)$  over the steady-state separation  $D(\infty) = \tilde{g}/\kappa$  as obtained from numerical integration under Eq. (9) as a function of time and for different tilt angles  $\Delta/\varepsilon_{d1}$ . As expected, for small  $\Delta/\varepsilon_{d1}$  the pointer states follow the ideal longitudinal dynamics expected from Eq. (12). c) Pointer state separation  $D(t)$  over the steady-state separation  $D(\infty)$  as found from numerical simulation of the system dynamics under the Hamiltonian of Eq. (15). Here,  $D(\infty)$  is numerically evaluated at long times and at small  $\Delta/\varepsilon_{d1}$ , corresponding to the average value of the bottom-right corner in panel (c). As in panel (b), the pointer state dynamics follow the expected behavior for small  $\Delta/\varepsilon_{d1}$ . The parameters used in panel (c) are  $\{\omega_a, \omega_b, \omega_c\}/2\pi = \{8.2, 5.2, 7.78\}$  GHz,  $\{\alpha_b/2, \alpha_c/2\}/2\pi = \{-0.17, 0.4\}$  GHz,  $\{g_a, g_b\}/2\pi = \{0.2, 0.2\}$  GHz,  $\tilde{c}_{d1}/2\pi = 0.7$  GHz and  $\kappa/2\pi = 0.05$  GHz.

To compare this Floquet longitudinal readout to the approach based on an adiabatic map followed by a dispersive readout of Refs. [3, 8, 29], we show in Fig. 2(a) the measurement pointer state separation [10]  $D(t) = |\langle \hat{a} \rangle_0(t) - \langle \hat{a} \rangle_1(t)|$ . This quantity is a helpful proxy for the signal-to-noise ratio (SNR) assuming a unit measurement-chain efficiency, as obtained from the expression [32]

$$\text{SNR}(T) = \sqrt{2\kappa \int_0^T D(t)^2 dt}. \quad (13)$$

In this expression,  $T$  is the measurement time,  $\kappa$  the decay rate of the cavity. For longitudinal coupling, this separation takes the simple form [14]

$$D(t) = \frac{\tilde{g}}{\kappa} \left(1 - e^{-\kappa t/2}\right). \quad (14)$$

The full blue lines in Fig. 2 correspond to longitudinal readout while the green lines to dispersive readout for which an expression equivalent to Eq. (14) can be obtained [14]. Comparing the full blue and full green lines, we see that longitudinal readout leads to much faster separation of the pointer states than dispersive readout even when ignoring the adiabatic mapping stage. When taking into account the required mapping stage (dashed green line), the advantage of the longitudinal approach over dispersive becomes even clearer. Here, we have used a mapping time of  $T_{\text{map}} = 30$  ns as in Ref. [3]. Finally, as a reference, the dashed blue line corresponds to a situation where the mapping stage is followed by a longitudinal readout. Although this would lead to a faster separation of the pointer state at short times as compared to the standard dispersive readout, we see that the main gain in the longitudinal Floquet readout introduced here comes from the fact that mapping to the laboratory frame qubit is no longer required.

As a further verification, Fig. 2(b) shows the pointer state separation  $D(t)$  as obtained from numerical integration of the system dynamics under the laboratory-frame Hamiltonian in Eq. (9) as a function of time and for different ratios  $\Delta/\varepsilon_{d1}$ . In the laboratory frame, we take the modulated coupling to be of the form  $g(t) = \tilde{g}[\cos(\omega_r t - \omega_0 t) + \cos(\omega_r t + \omega_0 t)]$ . In each simulation, the initial state of the cavity is chosen to be vacuum and the Floquet qubit state  $|\phi_0(0)\rangle$  or  $|\phi_1(0)\rangle$ . For ratios  $\Delta/\varepsilon_{d1} < 0.01$  (horizontal green dashed line), we find the expected exponential increase up to the steady-states  $D(\infty)$  in agreement with the analytical result of Eq. (14) shown in panel (a). On the other hand and as expected from the discussion below Eq. (9), when the Floquet qubit is too far away from resonance  $\Delta/\varepsilon_{d1} > 0.1$  (horizontal red dashed line), the separation between the pointer states does not follow the trajectory predicted by Eq. (14) and the readout is suboptimal.

## B. Superconducting circuit implementation

A possible realization of this longitudinal Floquet readout with superconducting quantum circuits is illustrated in Fig. 3. Here, a transmon qubit ( $\hat{b}$ ) is interaction with a readout cavity ( $\hat{a}$ ) via a flux-tunable coupler ( $\hat{c}$ ). This system can be modeled as a triplet of coupled Kerr oscillators [26]

$$H = H_a + H_b + H_c(t) + H_g + H_d(t), \quad (15)$$

where  $H_a = \omega_a \hat{a}^\dagger \hat{a}$  corresponds to the linear readout resonator, and  $H_b = \omega_b \hat{b}^\dagger \hat{b} + (\alpha_b/2) \hat{b}^{\dagger 2} \hat{b}^2$  to the transmon-like qubit with negative anharmonicity  $\alpha_b$ . The coupler Hamiltonian takes the same form  $H_c = \omega_c(t) \hat{c}^\dagger \hat{c} + (\alpha_c/2) \hat{c}^{\dagger 2} \hat{c}^2$ , except that it is parametrically modulated with  $\omega_c(t) = \omega_c + \delta\omega_c(t)$  using a time-dependent flux. The capacitive interactions are modeled by a linear off-diagonal Hamiltonian coupling the bare modes  $H_g =$

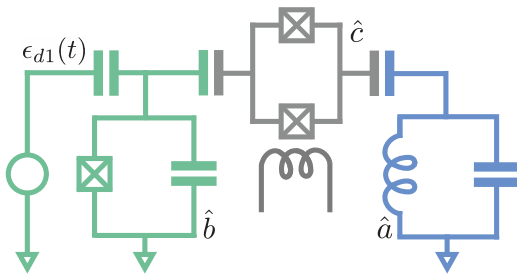


FIG. 3. Possible realization of the longitudinal Floquet readout. A driven transmon qubit (green) is coupled to a readout cavity (blue) via a flux modulated coupler (gray).

$\sum_{\alpha < \beta} g_{\alpha\beta} \hat{\alpha}^\dagger \hat{\beta} + \text{H.c.}$ , where the summation runs over the mode indices  $a, b, c$ . As shown in Appendix B, switching to a normal-mode representation, we can eliminate these bilinear terms to obtain the desired modulated coupling  $g(t)$  of Eq. (9) between the normal modes corresponding to the qubit and the readout resonator. This is achieved by modulating the coupler frequency at one or both of the sidebands  $\omega_a \pm \omega_b$ . Finally, the drive on the qubit takes the usual form  $H_d(t) = -i\varepsilon_{d1}(t)(\hat{b} - \hat{b}^\dagger)$ .

The coupling strength  $\tilde{g}$  depends on the three capacitive couplings, on the placement of the coupler frequency and on the amplitude of the modulation. Here, we choose this frequency to satisfy the constraint  $\omega_a < \omega_c < \omega_b$  to avoid excessive asymmetry. Figure 2(c) shows the pointer state separation under the evolution generated by Eq. (15) and with similar conditions and parameters to those used in panel (b). At  $\Delta/\varepsilon_{d1}$  small, we verify that the cavity pointer state displacement induced in the cavity by the readout of the Floquet States in the simulation of the full system Eq. (15) matches that of Hamiltonian Eq. (9). Importantly, the fast separation of the pointer states at short time is clearly observed.

## V. INITIALIZATION OF ARBITRARY FLOQUET STATES

In this section, we consider the timescale needed to initialize a Floquet qubit state with high fidelity. In particular, we point out that the adiabatic state transfer protocols of Refs. [8, 33] are not optimal in the regime advantageous for longitudinal Floquet readout, *i.e.*, small  $\Delta/\varepsilon_{d1}$ . Instead, we introduce an instantaneous ramping protocol which leads to high preparation fidelity in that regime.

### A. Adiabatic Regime

We first consider the timescale needed to initialize a Floquet qubit with a given fidelity in the adiabatic regime. More precisely, we consider an initial laboratory frame state  $\alpha|0\rangle + \beta|1\rangle$  and evaluate the fidelity

of the Floquet-state preparation protocol by projecting on the expected resulting Floquet state  $|\psi(T_{\text{ramp}})\rangle = \alpha|\phi_0(t)\rangle + \beta|\phi_1(t)\rangle$  after some ramp-up time  $T_{\text{ramp}}$  of the drive amplitude. Without loss of generality, we take  $\alpha = 1$  and  $\beta = 0$ , and compute the preparation fidelity  $\mathcal{F} = |\langle\psi(T_{\text{ramp}})|\phi_0(T_{\text{ramp}})\rangle|^2$  as a function of the ramp time  $T_{\text{ramp}}$  and for various ratios  $\Delta/\varepsilon_{d1}$  for the drive profile illustrated in Fig. 4(a).

Using a binary search in the range [1 ns, 3000 ns], we extract in Fig. 4(c) the minimal value for  $T_{\text{ramp}}$  corresponding to a fidelity  $\mathcal{F}$  larger than 99% (plain green), 99.9% (hatched green) and 99.99% (dotted green) for each ratio  $\Delta/\varepsilon_{d1}$ . We characterize the boundary of these empirical regions (dashed lines in log-log scale) by fitting an empirical law

$$T_{\text{ramp}} \times \left| \frac{\Delta}{\varepsilon_d} \right| \geq C_1, \quad (16)$$

where we find  $C_1 = 18.9$  ns for a 99% fidelity,  $C_1 = 28.4$  ns for 99.9%, and  $C_1 = 36.4$  ns for 99.99%, respectively. Extrapolating this proportionality relation closer to resonance  $\Delta = 0$ , we obtain the divergence of the adiabatic ramping time already observed in the context of driven two-body quantum systems [33]. In particular, for the small  $\Delta/\varepsilon_{d1}$  used in the longitudinal readout of the previous section, we find that the initialization is limited by the adiabatic lower bound  $T_{\text{ramp}} = C_1/0.01 = 1.9$  ms for a 99% fidelity and 2.8 ms for a 99.9% fidelity.

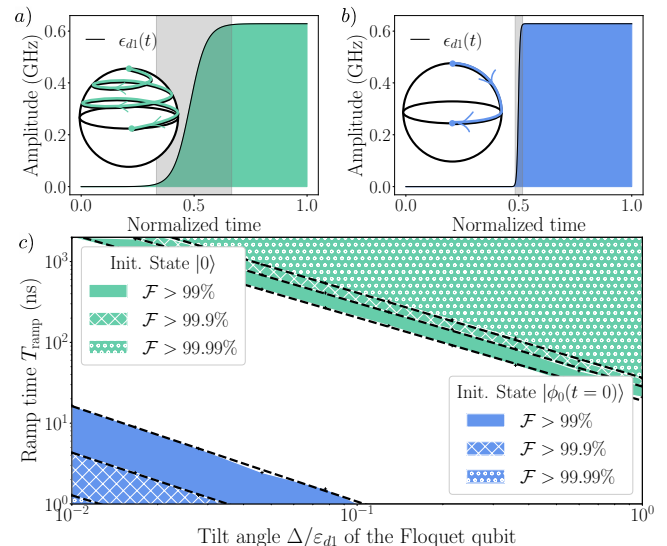


FIG. 4. Ramp profile for a) adiabatic and b) instantaneous preparation pulses, as well as illustrative paths on the Bloch sphere. The grey area can be used to compare the timescales involved in the two subplots. c) Initialization fidelity versus tilt angle  $\Delta/\varepsilon_{d1}$  and ramp time  $T_{\text{ramp}}$ . The different highlighted areas correspond to sectors where an initialization fidelity higher than 99% (plain), 99.9% (hatched) and 99.99% (dotted) can be obtained in the adiabatic limit (green) and the instantaneous (blue) regimes.

## B. Instantaneous regime

Because of the long preparation time required with small  $\Delta/\varepsilon_{d1}$  which is optimal for the longitudinal readout of Sec. IV, we now consider an alternative in the form of an instantaneous ramping protocol. Here, the main idea consists in preparing an initial superposition of the laboratory states  $\alpha|0\rangle + \beta|1\rangle$  that matches the instantaneous eigenstate  $|\phi_0(0)\rangle$  of the desired time-dependent Hamiltonian. An abrupt increase of the drive amplitude  $\varepsilon_{d1}(t)$ , as illustrated in Fig. 4(b), then connects the eigenstates  $|\phi_0(0)\rangle$  of the instantaneous Hamiltonian  $H(t_0)$  and the Floquet states  $|\phi_0(t)\rangle$  of the time-dependent Hamiltonian  $H(t)$ . The same idea can, in principle, be also used for the reverse mapping.

Computing again the fidelity of the protocol as a function of the ramp time and ratio  $\Delta/\varepsilon_{d1}$ , we find in Fig. 4(c) that the high-fidelity region (plain blue) is now delimited in parameter space by an upper bound in log-log scale rather than by a lower bound as was the case for the adiabatic protocol:

$$T_{\text{ramp}} \times \frac{\Delta}{\varepsilon_{d1}} \leq C_2, \quad (17)$$

where  $C_2 = 0.18$  ns for a 99% fidelity,  $C_2 = 0.06$  ns for 99.9%, and  $C_2 = 0.03$  ns for 99.99%, respectively. For the desired ratio  $\Delta/\varepsilon_{d1} = 0.01$  which led to a fast longitudinal readout, this corresponds to a ramp time of up to 18 ns (resp. 6 ns) to reach 99% (resp. 99.9%) fidelity. For larger ratios  $\Delta/\varepsilon_{d1} > 0.3$ , we were unable to reach convergence of the simulations, which indicates that the timescales involved are less than 1 ns.

## VI. SUMMARY

With the objective of identifying optimal gate parameters for Floquet qubits, we have shown how to define

the quasiphase spectra of a static system with two distinct drives and how to extract gate parameters from such spectra. To compensate for the computational cost of this approach, we use the semi-analytic Dysolve method for the integration of the unitary dynamics in our system [28]. In this way, we find a tenfold improvement in simulation time as compared to the QuTiP solver [34], opening up a path toward precise quasiphase spectra of complex quantum systems with two drives and a larger Hilbert space. Additionally, we introduce longitudinal Floquet readout which, in contrast with previous methods, does not require mapping the Floquet qubit to the laboratory-frame qubit before the measurement. This approach for readout of Floquet qubits completes the existing procedures for initialization, single-qubit gates and two-qubit gates, showing that quantum information processing on Floquet qubits is possible without having to come back to the underlying static undriven system. These results open new possibilities to further optimize gates and operations on Floquet qubits using the analytical understanding of the extended Floquet theory when only a few uncorrelated driving frequencies are involved. In future work, we will apply this framework to two-Floquet qubit gates with the objective of identifying optimal gate parameters with an approach that is free of approximations.

## ACKNOWLEDGMENTS

We thank Marie Lu, Jean-Loup Ville, and Joachim Cohen for a collaboration on a related topic and Zhiwen Huang, Jens Koch for stimulating discussions. This work was undertaken thanks to funding from NSERC, the Canada First Research Excellence Fund and the U.S. Army Research Office Grant No. W911NF-18-1-0411. This material is based upon work supported by the U.S. Department of Energy, Office of Science, National Quantum Information Science Research Centers, Quantum Systems Accelerator.

- 
- [1] D. Vion, A. Aassime, A. Cottet, P. Joyez, H. Pothier, C. Urbina, D. Esteve, and M. H. Devoret, Manipulating the Quantum State of an Electrical Circuit, *Science* **296**, 886 (2002).
  - [2] J. Koch, T. M. Yu, J. Gambetta, A. A. Houck, D. I. Schuster, J. Majer, A. Blais, M. H. Devoret, S. M. Girvin, and R. J. Schoelkopf, Charge-insensitive qubit design derived from the Cooper pair box, *Physical Review A* **76**, 042319 (2007).
  - [3] Z. Huang, P. S. Mundada, A. Gyenis, D. I. Schuster, A. A. Houck, and J. Koch, Engineering dynamical sweet spots to protect qubits from  $1/f$  noise, *Phys. Rev. Applied* **15**, 034065 (2021).
  - [4] N. Didier, Flux control of superconducting qubits at dynamical sweet spots, arXiv:1912.09416 [quant-ph] (2019), arXiv:1912.09416 [quant-ph].
  - [5] Q. Guo, S.-B. Zheng, J. Wang, C. Song, P. Zhang, K. Li, W. Liu, H. Deng, K. Huang, D. Zheng, X. Zhu, H. Wang, C.-Y. Lu, and J.-W. Pan, Dephasing-insensitive quantum information storage and processing with superconducting qubits, *Physical Review Letters* **10.1103/PhysRevLett.121.130501** (2018).
  - [6] N. Didier, E. A. Sete, J. Combes, and M. P. da Silva, AC flux sweet spots in parametrically-modulated superconducting qubits, *Physical Review Applied* **12**, 054015 (2019).
  - [7] J. A. Valery, S. Chowdhury, G. Jones, and N. Didier, Dynamical sweet spot engineering via two-tone flux modulation of superconducting qubits, arXiv:2104.07835 [quant-ph] (2021), arXiv:2104.07835 [quant-ph].
  - [8] P. S. Mundada, A. Gyenis, Z. Huang, J. Koch, and A. A. Houck, Floquet-engineered enhancement of coher-

- ence times in a driven fluxonium qubit, [Physical Review Applied](#) **14**, 054033 (2020), [arXiv:2007.13756](#).
- [9] C. Rigetti and M. Devoret, Fully microwave-tunable universal gates in superconducting qubits with linear couplings and fixed transition frequencies, [Phys. Rev. B](#) **81**, 134507 (2010).
- [10] A. Blais, A. L. Grimsmo, S. M. Girvin, and A. Wallraff, Circuit quantum electrodynamics, [Rev. Mod. Phys.](#) **93**, 025005 (2021).
- [11] T.-S. Ho, K. Wang, and S.-I. Chu, Floquet-Liouville supermatrix approach: Time development of density-matrix operator and multiphoton resonance fluorescence spectra in intense laser fields, [Physical Review A](#) **33**, 1798 (1986).
- [12] J. H. Shirley, Solution of the Schrödinger Equation with a Hamiltonian Periodic in Time, [Physical Review](#) **138**, B979 (1965).
- [13] H. Shill and J. V. Tietz, Semiclassical many-mode Floquet theory, . number **96**, 8 (1983).
- [14] N. Didier, J. Bourassa, and A. Blais, Fast quantum non-demolition readout from longitudinal qubit-oscillator interaction, [Physical Review Letters](#) **115**, 203601 (2015).
- [15] M. Grifoni and P. Hänggi, Driven quantum tunneling, [Physics Reports](#) **304**, 229 (1998).
- [16] S.-I. Chu and D. A. Telnov, Beyond the Floquet theorem: Generalized Floquet formalisms and quasienergy methods for atomic and molecular multiphoton processes in intense laser fields, [Physics Reports](#) **390**, 1 (2004).
- [17] A. Fainshtein and N. L. Manakov, Nonlinear susceptibilities and light scattering on free atoms, [Physics Reports](#) , 111 (1992).
- [18] M. Dörr, R. M. Potvliege, D. Proulx, and R. Shakeshaft, Multiphoton processes in an intense laser field. VI. Two-color ionization with incommensurable frequencies, [Physical Review A](#) **44**, 574 (1991).
- [19] P. J. D. Crowley, I. Martin, and A. Chandran, Topological classification of quasiperiodically driven quantum systems, [Physical Review B](#) **99**, 064306 (2019).
- [20] E. Boyers, P. J. D. Crowley, A. Chandran, and A. O. Sushkov, Exploring 2D synthetic quantum Hall physics with a quasi-periodically driven qubit, [Physical Review Letters](#) **125**, 160505 (2020).
- [21] D. M. Long, P. J. D. Crowley, and A. Chandran, Nonadiabatic topological energy pumps with quasiperiodic driving, [Phys. Rev. Lett.](#) **126**, 106805 (2021).
- [22] A. Poertner, *Bichromatic Dressing of Rydberg Atoms and on the Correctness of Many-Mode Floquet Theory*, Ph.D. thesis (2020).
- [23] T.-S. Ho and S.-I. Chu, Semiclassical many-mode Floquet theory. III. SU(3) dynamical evolution of three-level systems in intense bichromatic fields, [Physical Review A](#) **31**, 659 (1985).
- [24] T.-S. Ho and S.-I. Chu, Semiclassical many-mode Floquet theory: 11. Non-linear multiphoton dynamics of a two-level system in a strong bichromatic field, [Physics Reports](#) , 29 (1983).
- [25] A. N. Poertner and J. D. D. Martin, Validity of many-mode floquet theory with commensurate frequencies, [Phys. Rev. A](#) **101**, 032116 (2020).
- [26] A. Petrescu, C. Le Calonnec, C. Leroux, A. Di Paolo, P. Mundada, S. Sussman, A. Vrajitoarea, A. A. Houck, and A. Blais, Accurate methods for the analysis of strong-drive effects in parametric gates, [arXiv e-prints](#) (2021), [arXiv:2107.02343 \[quant-ph\]](#).
- [27] M. Mirrahimi and P. Rouchon, Dynamics and control of open quantum systems (2015).
- [28] R. Shillito, J. A. Gross, A. Di Paolo, É. Genois, and A. Blais, Fast and differentiable simulation of driven quantum systems, [arXiv:2012.09282 \[quant-ph\]](#) (2020), [arXiv:2012.09282 \[quant-ph\]](#).
- [29] C. Deng, J.-L. Orgiazzi, F. Shen, S. Ashhab, and A. Lupascu, Observation of floquet states in a strongly driven artificial atom, [Phys. Rev. Lett.](#) **115**, 133601 (2015).
- [30] A. Eddins, S. Schreppler, D. M. Toyli, L. S. Martin, S. Hacohe-Gourgy, L. C. G. Govia, H. Ribeiro, A. A. Clerk, and I. Siddiqi, Stroboscopic Qubit Measurement with Squeezed Illumination, [Physical Review Letters](#) **120**, 040505 (2018).
- [31] A. Grimm, N. E. Frattini, S. Puri, S. O. Mundhada, S. Touzard, M. Mirrahimi, S. M. Girvin, S. Shankar, and M. H. Devoret, The Kerr-Cat Qubit: Stabilization, Readout, and Gates, [Nature](#) **584**, 205 (2020).
- [32] C. C. Bultink, B. Tarasinski, N. Haandbaek, S. Poletto, N. Haider, D. J. Michalak, A. Bruno, and L. DiCarlo, General method for extracting the quantum efficiency of dispersive qubit readout in circuit QED, [Applied Physics Letters](#) **112**, 092601 (2018).
- [33] R. Desbuquois, M. Messer, F. Görg, K. Sandholzer, G. Jotzu, and T. Esslinger, Controlling the Floquet state population and observing micromotion in a periodically driven two-body quantum system, [Physical Review A](#) **96**, 053602 (2017).
- [34] J. Johansson, P. Nation, and F. Nori, QuTiP 2: A Python framework for the dynamics of open quantum systems, [Computer Physics Communications](#) **184**, 1234 (2013).



## Appendix A: Numerical approach for the Two-tone Floquet study

To obtain the quasiphase spectra in Fig. 1(c), we build the propagator associated with Eq. (8) for each ratio  $\omega_{d1}/\omega_{d2} = p/q$ . For a fixed numerator  $p$ , we sweep the denominator  $q$  and simulate the time dynamics over the period  $2\pi p/\omega_{d1}$ . For a TLS, diagonalization of the propagator then yields two eigenvalues on the unit circle, which correspond to two quasiphases in  $[-\pi, \pi]$ . Because of a sign ambiguity of the eigenvalues of the propagator, we fold the quasiphases in the interval  $[-\pi/2, \pi/2]$  to obtain the data points. In Fig. 5 we reproduce Fig. 1(c) now with 15 numerators to pinpoint the avoided crossing.

*Extracting gate parameters from discrete quasiphase spectra* – We identify the local minimum corresponding to the resonance using the following procedure:

1. For a first numerator  $p_0$ , vary the denominator  $q$  and find all discrete extrema of the quasienergy difference. Only one such extremum will correspond to the resonance while the others are a consequence of the folded space  $[-\pi/2, \pi/2]$ . We keep count of all successive triplets  $\{\phi_{p_0}[q-1], \phi_{p_0}[q], \phi_{p_0}[q+1]\}$  verifying  $\phi_{p_0}[q-1] \geq \phi_{p_0}[q]$  and  $\phi_{p_0}[q] \leq \phi_{p_0}[q+1]$ .
2. Given a new numerator  $p_k$ , we find all the triplets  $\{\phi_{p_k}[q'-1], \phi_{p_k}[q'], \phi_{p_k}[q'+1]\}$  as defined above such that the interval  $[\phi_{p_k}[q'-1], \phi_{p_k}[q'+1]]$  has a non-empty intersection with at least one such interval for  $k-1$ .
3. When the maximum numerator is reached, we expect to have discarded all the undesired local minima. The desired resonant frequency is located at the intersection of all ensembles:

$$\bigcap_{p_0 < p_k < p_{kmax}} [\phi_{p_k}[q_k-1], \phi_{p_k}[q_k+1]]. \quad (\text{A1})$$

The precision of the procedure is given by the range of this intersection. A simple upper bound for this quantity is the size of the smallest segment

$$\left( \frac{p_{kmax}}{q_{kmax}-1} - \frac{p_{kmax}}{q_{kmax}+1} \right) \approx \frac{2p_{kmax}}{q_{kmax}^2} \quad (\text{A2})$$

*Simulation times* – For the TLS studies in Sec. III B, the ratio was estimated to be  $\omega_{d1}/\omega_{d2} = p/q \approx 1/10$ . To achieve a precision of up to 1 MHz for the frequency  $\omega_{d2}$  maximizing the fidelity of the X-Gate, a maximum numerator greater than 20 is needed. To reach a precision of 0.1 MHz, the maximum numerator should rather be greater than 100. In that case, the propagator has to be calculated and diagonalized over 20 to 100 periods of the first drive and for each data point. For comparison, we used the solver for time unitary dynamics implemented in the Python Library QuTiP with custom

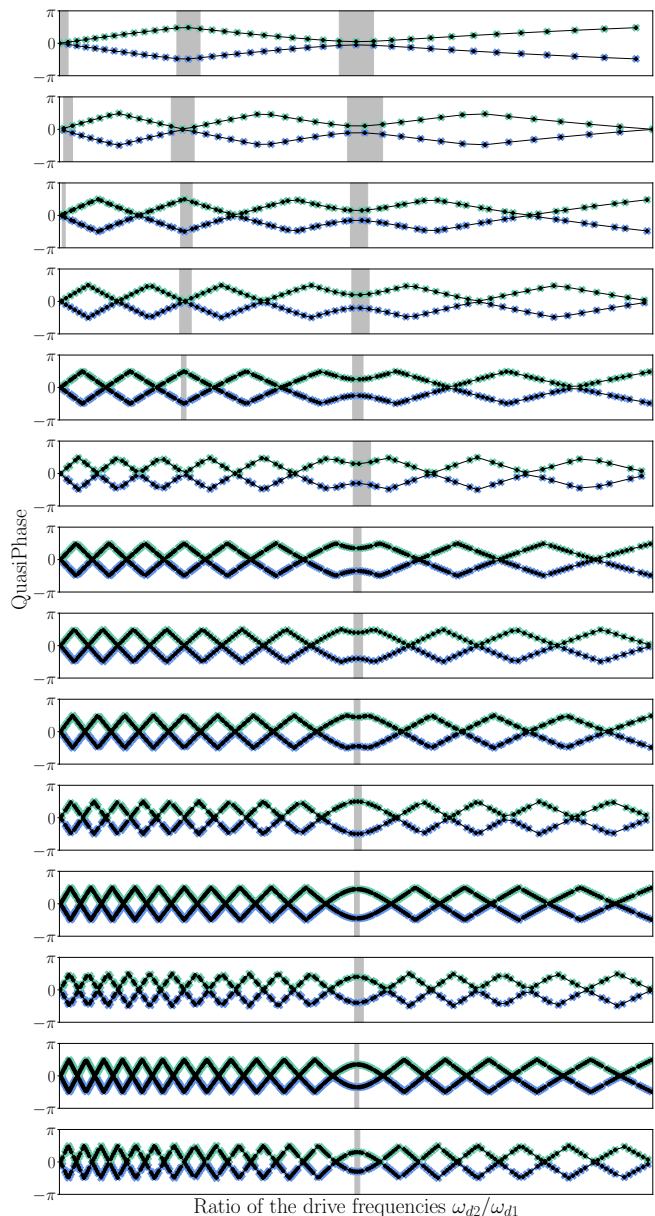


FIG. 5. Quasiphase spectrum for numerators  $1 \leq p_k \leq 15$ . The local minima of the avoided crossing can be observed on the first subplots and is characterized by a size  $p \times \varepsilon_{d2}$ . As this quantity goes beyond  $\pi/2$ , the local minimum becomes a local maximum in the folded space. The grey areas are used to visualize the triplet  $\{\phi_{p_k}[q'-1], \phi_{p_k}[q'], \phi_{p_k}[q'+1]\}$  corresponding to local extrema with a non-empty intersection to the grey areas in the above subplots.

options (atol=1e-10, rtol=1e-10, nsteps=1e9) for convergence [34].

With the objectives of reaching large numerators without loss of precision and of extending our study to systems with larger Hilbert space, we used the recent semi-analytic alternative *Dysolve* [28] which allows for efficient numerical simulation of system dynamics even in the presence of rapid oscillations.

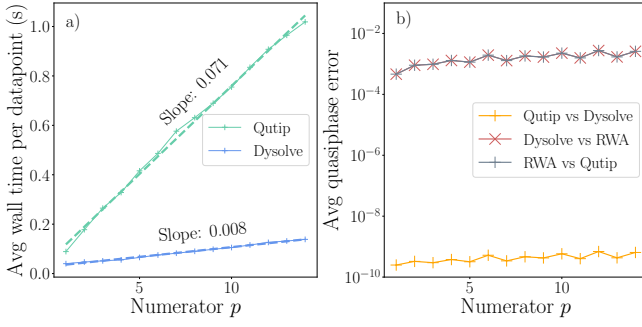


FIG. 6. a) Average wall time per data point for each numerator  $p$  using the reference solver QuTiP (green) and Dysolve (blue) [28]. Dashed lines are linear fits to the numerical results in continuous lines b) Comparison of the precision of the output for two numerical solvers and for the analytical solution in the RWA. The metric is the squared sum of the quasisphase difference for all data points corresponding to one numerator  $p$ . We find a good agreement between the two solvers (green) and we also highlight the poor precision of the analytical result based on the rotating-wave approximation (blue and orange), even for a TLS system.

In Fig. 6, we compare the performance of Dysolve with QuTiP's solver and report a tenfold improvement in simulation times with equivalent or better precision.

These gains open up a path toward precise quasisphase spectra of complex quantum systems with two drives and a large Hilbert space.

## Appendix B: Coupler-mediated qubit-readout cavity interaction

To achieve the coupling Hamiltonian in Eq. (9) for the longitudinal readout of a Floquet qubit, we consider the circuit in Fig. 3 where a coupler-mediated qubit-cavity interaction induces the desired readout. We first derive the Hamiltonian of the circuit without the voltage drive on the transmon, and then add the corresponding term.

It is the easiest to work in a bosonic representation and to consider a Kerr nonlinear oscillator model. The modes  $\hat{a}$ ,  $\hat{b}$ , and  $\hat{c}$  stand for readout resonator, qubit, and coupler, respectively. The three circuit elements are coupled capacitively and the Hamiltonian takes the form

$$H_{\text{lab}}(t) = \begin{pmatrix} \hat{a}^\dagger & \hat{b}^\dagger & \hat{c}^\dagger \end{pmatrix} \begin{pmatrix} \omega_a & g_{ab} & g_{ca} \\ g_{ab} & \omega_b & g_{bc} \\ g_{ca} & g_{bc} & \omega_c + \delta\omega_c(t) \end{pmatrix} \begin{pmatrix} \hat{a} \\ \hat{b} \\ \hat{c} \end{pmatrix} + \frac{\alpha_b}{2} \hat{b}^{\dagger 2} \hat{b}^2 + \frac{\alpha_c}{2} \hat{c}^{\dagger 2} \hat{c}^2. \quad (\text{B1})$$

Here,  $\alpha_b$  and  $\alpha_c$  are the qubit and coupler anharmonicities, respectively. The coupler is modulated parametrically with  $\delta\omega_c(t)$  which is a yet-unspecified function of time, with the sole requirement that it contains no dc part:  $\lim_{T \rightarrow \infty} \frac{1}{T} \int_0^T \delta\omega_c(t) dt = 0$ .

A normal-mode transformation diagonalizes the time-independent part of the quadratic Hamiltonian. Let us denote the hybridization coefficients of this transformation by  $\hat{\beta} = \sum_{\alpha=a,b,c} u_{\beta\alpha} \hat{\alpha}$ , for  $\beta = a, b, c$ . With this, the Hamiltonian consists of a diagonal quadratic form determined by the qubit, cavity, and coupler-like normal mode frequencies

$$H^{(0)} = \omega_a \hat{a}^\dagger \hat{a} + \omega_b \hat{b}^\dagger \hat{b} + \omega_c \hat{c}^\dagger \hat{c}, \quad (\text{B2})$$

and a perturbation coming from the quartic terms and the time-dependent modulation of the coupler

$$\lambda H^{(1)}(t) = \sum_{j=b,c} \frac{\alpha_j}{2} \left( \sum_{\alpha=a,b,c} u_{j\alpha} \hat{\alpha}^\dagger \right)^2 \left( \sum_{\alpha=a,b,c} u_{j\alpha} \hat{\alpha} \right)^2 + \delta\omega_c(t) (u_{ca} \hat{a}^\dagger + u_{cb} \hat{b}^\dagger + u_{cc} \hat{c}^\dagger) (u_{ca} \hat{a} + u_{cb} \hat{b} + u_{cc} \hat{c}). \quad (\text{B3})$$

The coupling in Eq. (9) can be attained by identifying  $g(t) = u_{ca} u_{cb} \delta\omega_c(t)$ , and making all other terms in  $g(t)$  but  $a^\dagger b + b^\dagger a$  vanish in the RWA. Moreover, one can find the resulting anharmonicities of all three modes, as well as the cross-Kerr interactions, in the RWA

$$\alpha_j^{(1)} = \sum_{i=b,c} u_{ij}^4 \bar{\alpha}_i, \quad \chi_{jk}^{(1)} = \sum_{i=b,c} 2u_{ij}^2 u_{ik}^2 \bar{\alpha}_i. \quad (\text{B4})$$

Finally, the following term is added to the Hamiltonian to account for the yet missing qubit drive:

$$H_d(t) = -i\epsilon_d(t) (\hat{b} - \hat{b}^\dagger) = -i\epsilon_d(t) \sum_{\alpha=a,b,c} u_{b\alpha} (\hat{\alpha} - \hat{\alpha}^\dagger), \quad (\text{B5})$$

which accounts for the control signals sent to the qubit that are off-resonantly driving the remaining two normal modes. These contributions are typically negligible.